Frequency domain photothermal radiometry with spherical solids

Chinhua Wang[a)]
Institute of Modern Optical Technologies, Suzhou University, Suzhou, Jiangsu 215006, People's Republic of China and Key Lab of Modern Optical Technologies of Jiangsu Province, Jiangsu, People's Republic of China

Yue Liu and Andreas Mandelis
Center for Advanced Diffusion Wave Technologies, Department of Mechanical and Industrial Engineering, University of Toronto, Toronto M5S 3G8, Canada

Jun Shen
National Research Council of Canada, Institute for Fuel Cell Innovation, 4250 Wesbrook Mall, Vancouver, British Columbia V6T 1W5, Canada

(Received 24 January 2007; accepted 25 February 2007; published online 16 April 2007)

Motivated by increasing practical and industrial applications of photothermal techniques in the measurement of materials of various shapes with curvature, we extend the applications of photothermal diagnostics to solid spheres, in which both theoretical and experimental photothermal radiometry studies on spherical geometries and thermal diffusivity of the sample are discussed. Based on the Green function method, a full thermal-wave field distribution of a spherical solid is obtained. The characteristics of the thermal-wave field with respect to thermophysical properties of the material, the diameter of the solid, the size of the incident laser beam, and the measurement angle are discussed. Experimental results with steel spheres of different diameters exhibit good agreement between the theory and the experiments. © *2007 American Institute of Physics*. [DOI: 10.1063/1.2721424]

I. INTRODUCTION

Due to its noncontact, nondestructive, and highly sensitive nature, photothermal radiometry (PTR) has become a powerful tool for the thermal characterization and nondestructive evaluation of broad classes of materials[1–5] since the late 1980s. Photothermal radiometry is based on the generation and detection of thermal waves in a sample as a result of absorption and nonradiative conversion of an intensity modulated laser beam. The laser-induced oscillating temperature distribution in the solid results in changes in infrared radiation emission from the material which can be quantitatively evaluated by the Stefan–Boltzmann law. For decades, however, studies in photothermal techniques have been restricted to samples with flat surfaces, for which either a one-dimensional[3] or a three-dimensional[5,6] theoretical model has been developed and applied in various material studies, depending on the relative size of incident beam spot size and thermal diffusion length within the modulation frequency range of interest. With recently increasing applications of PTR to the nondestructive evaluation of industrially manufactured products, requirements for characterization of samples with curvature, such as cylinders and spheres, have made it necessary to consider the formulation of thermal-wave fields in curvilinear coordinate systems. As a result, PTR has been extended to quantitative evaluation of both homogeneous and composite cylindrical structures.[7,8] Theoretical studies and experimental validation have been performed in the frequency domain. Salazar *et al.*[9] further verified and developed the PTR technique in the time domain in which the thermal diffusivity of cylindrical rods and tubes was evaluated using the flash method. Salazar *et al.*[9] also derived the thermal-wave [alternating current (ac) temperature] field of a spherical solid in which the sample is assumed to be illuminated by a collimated beam with a spot size equal to the diameter of the spherical sample. In this article, we extend the PTR technique to spherical samples excited by a laser beam of arbitrary spot size. Specifically, we present both theoretical and experimental PTR studies on spherical solids in the frequency domain. Based on the Green function method,[10] the thermal-wave field distribution of a spherical surface under the excitation of a periodically modulated uniform beam is obtained. The characteristics of the thermal-wave field related to various material parameters and beam sizes are discussed. Finally, the theoretical model is further validated experimentally with spherical steel samples of different diameters.

II. THEORY

The thermal-wave field in a spherical sample of radius R_0, induced by modulated optical excitation of the spherical surface, can be conveniently derived based on the Green function method. The geometry and the coordinates of the boundary-value problem are shown in Fig. 1. The exciting laser beam, which is of circular symmetry with respect to the z axis and subtends an angle ψ, impinges uniformly on the spherical surface, in conformity with typical experimental geometries. Considering the harmonic modulation of the incident exciting light, the governing thermal-wave equation for the material under investigation can be written as

$$\nabla^2 T(\mathbf{r},\ \omega) - \sigma^2(\omega) T(\mathbf{r},\omega) = -\frac{1}{k} Q(\mathbf{r},\omega), \tag{1}$$

[a)]Electronic mail: chinhua.wang@suda.edu.cn

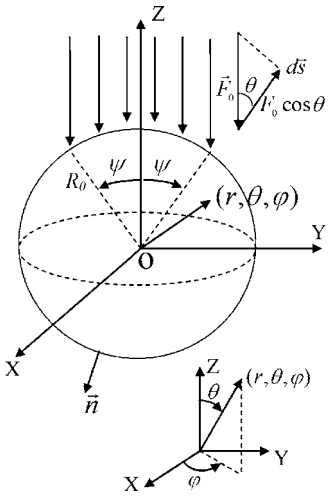

FIG. 1. Geometry of a solid sphere of radius R_0 externally excited photothermally by a uniform light beam impinging on part of its surface subtending a sector of angle 2ψ. Inset: spherical coordinate system used in this work.

where $\sigma(\omega)=(i\omega/\alpha)^{1/2}=(1+i)\sqrt{\omega/2\alpha}$ is the thermal wave number; α (m^2/s) and k (W/K m) are, respectively, the thermal diffusivity and the thermal conductivity of the material; ω is the angular modulation frequency, and $Q(\mathbf{r},\omega)$ is the volume thermal source at coordinates (r,φ) inside the material. Based on the Green function method, the general solution for Eq. (1) can be expressed as[10]

$$T(r,\omega)=(\alpha/k)\int\int\int_{V_0} Q(\mathbf{r}_0,\omega)G(\mathbf{r}|\mathbf{r}_0;\omega)dV_0 + \alpha\oint_{s_0}[G(\mathbf{r}|\mathbf{r}_0^s;\omega)\nabla_0 T(\mathbf{r}_0^s;\omega) - T(\mathbf{r}_0^s,\omega)\nabla_0 G(\mathbf{r}|\mathbf{r}_0^s;\omega)]d\mathbf{S}_0, \quad (2)$$

where S_0 is the surface surrounding the domain volume V_0, which includes the harmonic source $Q(\mathbf{r}_0,\omega)$. $\mathbf{r}_0^s$ is a position vector from the origin representing the coordinate of a source point on surface S_0. $d\mathbf{S}_0$ indicates an infinitesimal area vector along the outward direction normal to the boundary surface S_0: $d\mathbf{S}_0=\mathbf{n}dS_0$ with $\mathbf{n}$ being the outward unit vector, as shown in Fig. 1. $G(\mathbf{r}|\mathbf{r}_0;\omega)$ is the thermal-wave Green function with units (s/m^3). The physical interpretation of this particular Green function, as opposed to conventional heat-diffusion Green functions[11,12] is that it represents the temperature modulation anywhere in a given domain due to a harmonic heat source of unit strength located at point $\mathbf{r}=\mathbf{r}_0$ within the domain and represented by the Dirac delta function $\delta(\mathbf{r}-\mathbf{r}_0)$.[10] The Green function $G(\mathbf{r}|\mathbf{r}_0;\omega)$ takes different forms depending on the types of boundary conditions, e.g., Dirichlet, Neumann, or mixed (third-kind), imposed on the investigated material.

In the most general case, when a laser beam is incident onto a homogeneous solid which is not entirely opaque, the material will absorb some of the photon energy and thus generate a volume heat source. Depending on the surface of the material, different types of the boundary conditions may apply. Therefore, the temperature field must be evaluated using the complete form of Eq. (2). However, in most cases, Eq. (2) can be simplified depending on specific material properties. For solids with high attenuation of the incident light, such as metals, the absorption of the incident light occurs at the surface, and therefore, the volume source can be neglected. In this article, we will focus on opaque materials. In the absence of a volume source, and assuming the system is subject to boundary conditions of the third kind, we obtain

$$Q(\mathbf{r}_0,\omega)=0, \quad (3a)$$

$$k\mathbf{n}\cdot\nabla T(\mathbf{r},\omega)|_{r=r^s}+HT(\mathbf{r}^s,\omega)=F(\mathbf{r}^s,\omega), \quad (3b)$$

$$k\mathbf{n}\cdot\nabla G(\mathbf{r}|\mathbf{r}_0;\omega)|_{r=r^s}+HG(\mathbf{r}^s|\mathbf{r}_0;\omega)=0, \quad (3c)$$

where H is the heat transfer coefficient representing convective heat loss and $F(\mathbf{r}^s,\omega)$ is the thermal flux distribution along the spherical bounding surface. Substituting Eq. (3a)–(3c) into Eq. (1) yields

$$T(\mathbf{r},\omega)=\left(\frac{\alpha}{k}\right)\oint_{s_0} G(\mathbf{r}|\mathbf{r}_0^s;\omega)F(\mathbf{r}_0^s,\omega)dS_0. \quad (4)$$

Assuming that the intensity of the incident radiation on the surface is uniform, in conformity with our PTR system, the thermal flux, which must be weighed by a projection factor in the form of the cosine of the angle with the direction of the incident light intensity, can be expressed as

$$F(R_0,\theta,\varphi;\omega)=\begin{Bmatrix}(1/2)F_0\cos\theta[1+\exp(i\omega t)];\ 0\le\theta\le\psi,\ 0\le\varphi\le 2\pi\\ 0;\ \psi\le\theta\le\pi,\ 0\le\varphi\le 2\pi.\end{Bmatrix} \quad (5)$$

From the symmetry of the boundary value problem, it is expected that the thermal-wave field will be symmetric with respect to the z axis. The appropriate Green function corresponding to the foregoing boundary condition is[10]

$$G(r,\theta|r_0,\theta_0;\omega)=\frac{i\kappa}{2\pi\alpha}\begin{cases}\sum_{l=0}^{\infty}\left\{\frac{[h_l^{(1)}(\kappa r_0)f_l^{(2)}(\kappa R_0)-f_l^{(1)}(\kappa R_0)h_l^{(2)}(\kappa r_0)]j_l(\kappa r)}{f_l^{(1)}(\kappa R_0)+f_l^{(2)}(\kappa R_0)}\right\}N_l(\theta)N_l(\theta_0),\ 0\le r\le r_0\\ \sum_{l=0}^{\infty}\left\{\frac{[h_l^{(1)}(\kappa r)f_l^{(2)}(\kappa R_0)-f_l^{(1)}(\kappa R_0)h_l^{(2)}(\kappa r)]j_l(\kappa r_0)}{f_l^{(1)}(\kappa R_0)+f_l^{(2)}(\kappa R_0)}\right\}N_l(\theta)N_l(\theta_0),\ r_0\le r\le R_0\end{cases}, \quad (6)$$

with $f_l^{(1,2)}$ defined as

$$f_l^{(1,2)}(\kappa r) \equiv h_l^{(1,2)}(\kappa r) + \left(\frac{k}{H}\right)\frac{d}{dr}h_l^{(1,2)}(\kappa r), \tag{7}$$

where $h_l^{(1,2)}(\kappa r)$ are the complex spherical Hankel functions of the third kind and of order l. They can be defined as $h_l^{(1,2)}(z) \equiv j_l(z) \pm i n_l(z)$, where $j_l(z)$and $n_l(z)$ are the complex-argument spherical Bessel functions of the first and the second kind, respectively, of order l. $N_l(\theta) = \sqrt{(2l+1)/2}P_l(\cos\theta)$, where $P_l(\cos\theta)$ is a Legendre polynomial, and $\kappa(\omega)$is a modified complex thermal wave number: $\kappa(\omega) \equiv i\sigma = -(1-i)\sqrt{\omega/2\alpha}$.

Neglecting the direct current term in Eq. (5), interchanging r and r_0, $\mathbf{r} \Leftrightarrow \mathbf{r}_0$, and noting the azimuthal isotropy of the problem, Eq. (4) can be further expressed in the form

$$T(\mathbf{r},\omega) = \frac{iF_0R_0^2\kappa}{2k}\sum_{l=0}^{\infty}\frac{[h_l^{(1)}(\kappa R_0)f_l^{(2)}(\kappa R_0) - f_l^{(1)}(\kappa R_0)h_l^{(2)}(\kappa R_0)]j_l(\kappa r)}{f_l^{(1)}(\kappa R_0) + f_l^{(2)}(\kappa R_0)}N_l(\theta)j_l(\kappa r)\int_0^{\psi}N_l(\theta_0)\sin\theta_0\cos\theta_0 d\theta_0. \tag{8}$$

By integrating the last term in Eq. (8) and separating out the $l=0$ and $l=1$ terms for computational convenience, the thermal-wave field can be expressed analytically as

$$\begin{aligned}T(\mathbf{r},\omega) = \frac{F_0}{2k}\Bigg\{ & \frac{j_0(\kappa r)}{\frac{HA}{k} + \frac{(\sigma R_0 - 1)}{\sigma R_0^2}e^{\sigma R_0}\left[1 - \frac{1+\sigma R_0}{1-\sigma R_0}e^{-2\sigma R_0}\right]}\frac{\sin^2\psi}{2} \\ & + \frac{j_1(\kappa r)}{\frac{Hj_1(\kappa R_0)}{k} + \frac{d}{dr}[j_1(\kappa R_0)]}\frac{\cos\theta}{2}(1-\cos^3\psi) \\ & - \frac{\sin\psi}{2}\sum_{l=2}^{\infty}\frac{j_l(\kappa r)P_l(\cos\theta)}{\frac{Hj_l(\kappa R_0)}{k} + \frac{d}{dr}[j_l(\kappa R_0)]}\frac{(2l+1)}{(l-1)(l+2)} \\ & \times[\sin\psi P_l(\cos\psi) + \cos\psi P_l^1(\cos\psi)]\Bigg\},\end{aligned} \tag{9}$$

where $A = (e^{i\kappa R_0} - e^{-i\kappa R_0})/i\kappa R_0$ and P_l^m are the associated Legendre polynomials and $(d/dz)j_l(z) \equiv j_l'(z)$ is the derivative of the spherical Bessel function given by

$$j_i'(z) = \frac{1}{2l+1}[lj_{l-1}(z) - (l+1)j_{l+1}(z)]. \tag{10}$$

Equation (9) gives a general solution of the boundary value problem under the third kind boundary condition with heat transfer coefficient H ranging from 0 to ∞. Note that in the absence of heat losses, $H=0$, the third kind boundary condition reduces to the second kind (Neumann) adiabatic boundary condition, which appears to be the case in most experimental conditions. It can be justified by the small heat-transfer coefficient $H(\sim 0.1\ \mathrm{W/m^2\ K})$ between the material and the static air in typical laboratory settings and by the small temperature difference between the sample and the ambient medium ($\ll 1$ K) when compared with the incident heat flux $F(R_0,\theta,\omega)$ ($\sim 10^5\ \mathrm{W/m^2}$ for a 1 W laser beam with a 10 $\mathrm{mm^2}$ spot size). Moreover, in our experiments, neglecting the heat-transfer term can also be justified by the very small (~ 0.1) Grashoff (Gr) number. Free convection is effectively suppressed when $\mathrm{Gr} < 2000$.[13] Therefore, Eq. (9) can further be simplified as

$$\begin{aligned}T(\mathbf{r},\omega) = \frac{F_0}{2k}\Bigg\{ & \frac{j_0(\kappa r)e^{-\sigma R_0}\sigma R_0^2}{(\sigma R_0 - 1)\left[1 - \frac{1+\sigma R_0}{1-\sigma R_0}e^{-2\sigma R_0}\right]}\frac{\sin^2\psi}{2} \\ & + \frac{j_1(\kappa r)}{\frac{d}{d(\kappa r)}[j_1(\kappa R_0)]}\frac{\cos\theta}{2\kappa}(1-\cos^3\psi) \\ & - \frac{\sin\psi}{2\kappa}\sum_{l=2}^{\infty}\frac{j_l(\kappa r)}{\frac{d}{d(\kappa r)}[j_l(\kappa R_0)]}\frac{P_l(\cos\theta)(2l+1)}{(l-1)(l+2)} \\ & \times[\sin\psi P_l(\cos\psi) + \cos\psi P_l^1(\cos\psi)]\Bigg\}.\end{aligned} \tag{11}$$

Equation (11) gives the thermal-wave field at any point inside the spherical solid. From the structure of this expression it is seen that the frequency dependence of the thermal-wave field of spheroids under illumination by a uniform light beam is a strong function of the material thermal diffusivity as well as geometrical factors of the solid. As shown in Eq. (11), if $\psi=0$, i.e., no light is incident on the surface, the temperature field $T(\mathbf{r},\omega)=0$, as expected. If $\psi=90°$, i.e., full hemispherical illumination, the thermal-wave field reduces to:

$$\begin{aligned}T(\mathbf{r},\omega) = \frac{F_0}{2k}\Bigg\{ & \frac{j_0(\kappa r)e^{-\sigma R_0}\sigma R_0^2}{2(\sigma R_0 - 1)\left[1 - \frac{1+\sigma R_0}{1-\sigma R_0}e^{-2\sigma R_0}\right]} \\ & + \frac{j_1(\kappa r)}{\frac{d}{d(\kappa r)}[j_1(\kappa R_0)]}\frac{\cos\theta}{2\kappa} - \frac{1}{2\kappa} \\ & \times\sum_{l=2}^{\infty}\frac{j_l(\kappa r)}{\frac{d}{d(\kappa r)}[j_l(\kappa R_0)]}\frac{P_l(\cos\theta)(2l+1)}{(l-1)(l+2)}[P_l(0)]\Bigg\}.\end{aligned} \tag{12}$$

III. NUMERICAL CALCULATIONS

Equation (11) shows a very complicated relationship between the modulated temperature field and the thermophysical parameters, as well as several geometric and measurement configuration factors for a spherical solid. To gain more

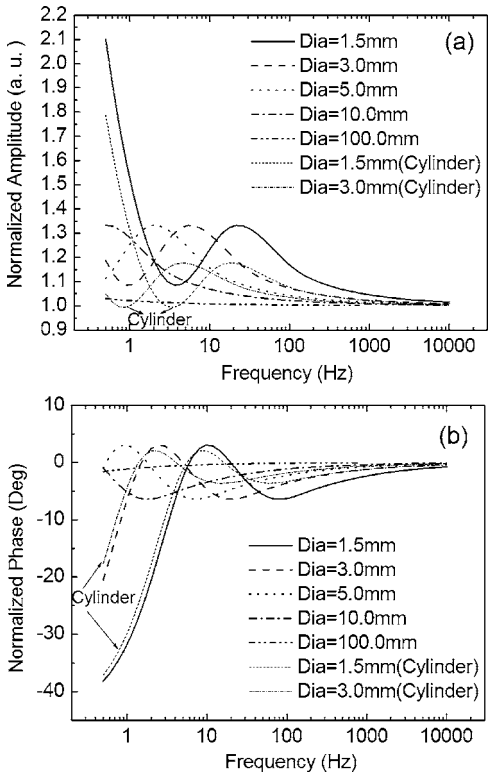

FIG. 2. Effect of the diameter of the spherical solid on the thermal-wave field measured at the sample surface ($r=R_0$) and angle $\theta=0°$. The illuminating laser beam size subtends an angle of $\psi=90°$. Amplitude and phase are normalized, respectively, to the corresponding values of a flat semi-infinite surface of the same material.

physical insight into the characteristics of the thermal-wave field, it is instructive to study its dependence on individual parameters involved in Eq. (11). Considering the nature of PTR measurements of opaque solids, only the thermal-wave field on the sample surface ($r=R_0$) will be evaluated in the following simulations. In all simulations, the amplitude and the phase of the surface temperature oscillation are normalized to the corresponding amplitude and phase of a flat surface of a semi-infinitely thick sample of the same material in order to see the effects of the curved surface with optimal contrast. The normalization process involves amplitude ratios and phase differences. The amplitude and phase of a flat surface are calculated based on the well-known one-dimensional (1D) theoretical model of thermal waves, valid under the condition that the incident beam spot size is much larger than the thermal diffusion length of the material within the modulation frequency range of interest. Under illumination producing a constant-amplitude thermal-wave flux F_0 at the surface of the flat sample, the ac temperature field evaluated at the surface is given by the well-known dependence of the amplitude on the inverse of the square root of the frequency and a constant $(\pi/4)$ phase lag of the temperature oscillation with respect to the incident thermal flux.[10]

Figure 2 shows the effect of the diameter of a spherical solid on the thermal-wave field measured at the sample surface ($r=R_0=3$ mm) and at angle $\theta=0°$. The beam size is assumed to be large enough so as to cover the entire upper part of the sphere, therefore, $\psi=90°$ is assumed in the calculation or Eq. (12) is used directly. The other material parameters used in the simulation are as follows: $\alpha=13.57\times10^{-6}$ m^2/s for AISI 1018 carbon steels,[14] $F_0=1$ W/cm^2, and $k=51.9$ W/K m.

It is seen that, as the diameter of the sphere increases, both the normalized amplitude and phase curves become flatter, an indication that the thermal-wave field from large diameter of spheres reduces gradually to that of a flat surface, as expected. As shown in Figs. 2(a) and 2(b), amplitude and phase reduces to a flat line toward 1 and 0, respectively, when the diameter is equal to 100 mm. It is also noted that when the diameter of the sphere is small, e. g., $2R_0<5$ mm, both amplitude and phase exhibit peaks as a function of modulation frequency which shift to lower frequency values with increasing diameter. The origin of the peaks in amplitude and phase is akin to resonances observed in propagating (i.e., nondiffusive) wave fields and can be attributed to thermal wave interference within the confined geometry of the spherical solid, a physical explanation similar to that of cylindrical geometries.[7] The boundary of the finite-diameter sphere confines the thermal waves and forms a low-Q resonant material cavity,[15] as witnessed by the stronger interference effect in the smaller diameter spheres. All the amplitude and phase curves at high frequencies converge to 1 and 0, respectively, the behavior of a flat surface. This can be explained by the shorter thermal diffusion length at higher modulation frequencies which favors the forward conduction pathway compared to other (sideways) degrees of freedom. The larger ratio, R, of the surface curvature radius to thermal diffusion length at higher frequencies is closer to that of a flat surface, for which $R\rightarrow\infty$. In Fig. 2 we also show simulation results of cylindrical C1018 rods of the same diameters as the corresponding spherical C1018 samples for comparison (diameter=1.5 and 3.0 mm, respectively). It is interesting to see that both normalized amplitude and phase of the spherical samples show larger magnitude of oscillations than that of the cylindrical samples of the same diameter. For the sample of 1.5-mm diameter, the normalized amplitude of the spherical sample oscillates from 2.1 at 0.5 Hz to 1.08 (trough) at ~3.7 Hz and then to 1.34 (peak) at ~22 Hz while the amplitude of the cylindrical sample oscillates from 1.79 at 0.5 Hz to ~1 at ~3.2 Hz (trough) and then to 1.17 (peak) at ~18 Hz. The corresponding peak/trough of the cylindrical sample shows a shift toward lower frequencies than that of the spherical sample. The same trend is apparent in the phase channel, in which the magnitude of the oscillation of the normalized phase of the spherical sample is larger than the corresponding cylindrical sample. This can be qualitatively explained by the geometrical fact that the spherical sample is effectively a higher Q-parameter cavity than the cylindrical sample. The finite extent of the spherical surface forms a closed (confined) circular thermal-wave cavity while the surface of the cylindrical sample forms a closed thermal-wave cavity only along the radial direction. Therefore, the thermal wave confinement inside a spherical sample is better than that of a cylindrical sample, thus exhibiting larger magnitude of oscillation than the cylindrical sample.

Figures 3 and 4 show the frequency dependence of spherical thermal-wave fields on the spherical surface (diameter=3.0 mm) at various longitudinal angles θ when

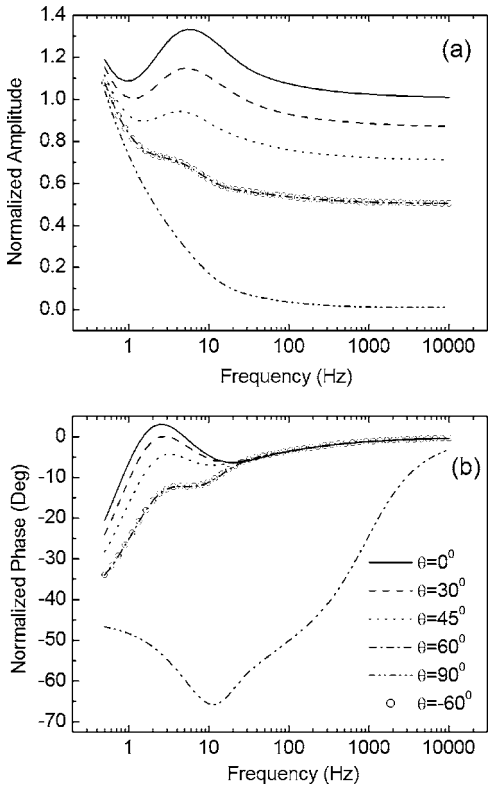

FIG. 3. The normalized surface thermal-wave amplitude and phase ($r=R_0$) at various measurement angles (upper part of the sphere, $-90° \leq \theta \leq 90°$) for a sphere with a diameter of 3.0 mm. The illuminating beam size subtends an angle of $\psi=90°$. Both amplitude and phase plots use the same symbol notations for different angles.

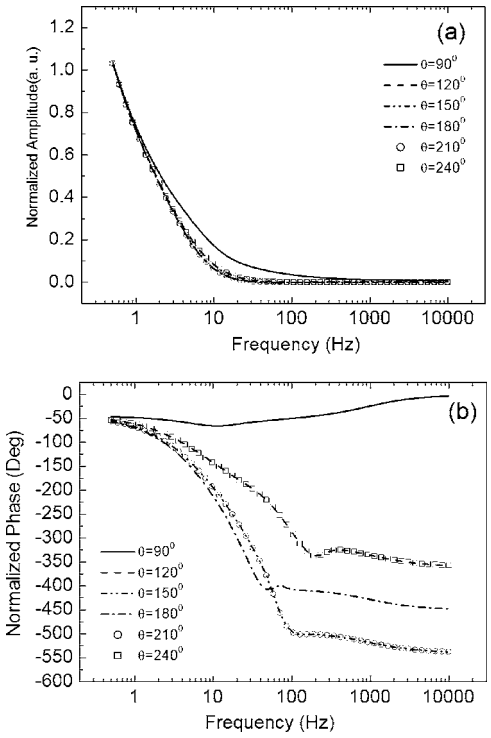

FIG. 4. The normalized surface thermal-wave amplitude and phase ($r=R_0$) at various measurement angles (lower part of the sphere, $90° \leq \theta \leq 270°$) for a sphere with a diameter of 3.0 mm. The illuminating beam size subtends an angle of $\psi=90°$. Both amplitude and phase plots use the same symbol notations for different angles.

the illumination of the incident beam is expanded to cover the whole upper part of the sphere (i.e., $\psi=90°$). The temperature fields plotted in Figs. 3 and 4 represent two different PTR measurement schemes, i.e., reflection (backpropagation) and transmission modes, respectively. In reflection PTR, the signal is measured in the upper region of the sphere ($-90° < \theta < 90°$) which is on the same side as the incident illumination, while in transmission PTR the signal is measured in the lower region of the sphere ($90° < \theta < 270°$), on the side opposite to the illuminated surface. In a manner similar to cylindrical geometries,[7,8] both amplitude and phase strongly depend on the measurement angle θ. Although the incident beam is uniform and expanded to cover the entire upper part of the sphere, the thermal flux absorbed by the sphere is a projection of the incident uniform flux normal to the spherical surface with the angle θ along the curved surface in the upper part of the sphere. At different angles, the frequency dependence of the PTR signal is different. In Fig. 3, both amplitude and phase are very sensitive to the angular coordinate θ. The PTR amplitude near $\theta=0°$ exhibits a stronger thermal-wave interferometric peak than that near 90° or −90°, as shown in Fig. 3(a) for different θ. This is due to the weaker strength of the thermal-wave field at positions near + 90° or −90°. (The net photothermal flux into the sphere decreases as $\mathbf{F}\cdot\mathbf{dS}$ decreases at large polar angles, Fig. 1.) This explains the decreased amplitude with increasing angle θ in Fig. 3(a). At $\theta \sim \pm 90°$, $\mathbf{F}\cdot\mathbf{dS}=0$ and the formation of a thermal standing wave is not possible, due to the infinite effective thickness of the cavity formed by the upper and lower sectors of the spherical surface along the z axis of symmetry at $\theta=0°$. The amplitude interference peak disappears in Fig. 4 when the PTR signal is measured in the transmission mode (i.e., $90° < \theta < 270°$). This is consistent with the heavy attenuation of the interfering waves after double thermal transit across the body of the sphere. The phase in Fig. 4 shows a stronger dependence on frequency than that in the reflection mode, Fig. 3. Due to the symmetry of illumination about the 0° axis perpendicular to the surface, the thermal-wave field also exhibits symmetry, as can be seen from the coincidence of the frequency scan curves at $\theta=60°/-60°$ in Fig. 3 and $\theta=120°/240°$, and 150°/210° in Fig. 4, as expected.

Figure 5 is a simulation showing the effect of laser-beam size on the thermal-wave field at $\theta=0°$ using parameters of a C1018 steel sample with a diameter of 3 mm. The normalization is still performed with the thermal-wave field of a 1D flat solid with the same thermophysical properties. It is seen that the amplitude peak decreases at decreasing angles ψ due to the increasing remoteness of the spherical boundaries from the thermal-wave flux: boundaries are thermal-wave confining interfaces which induce interferometric superposition of thermal waves across the volume of the spheroid and their increasingly remote location from the thermal-wave source diminishes the effects of superposition. The peak shifts to higher frequencies at smaller optothermal aperture ψ, as the effective distance to the solid-air boundary decreases, with only the immediately adjacent curved surface to the illuminated region contributing to the confinement of

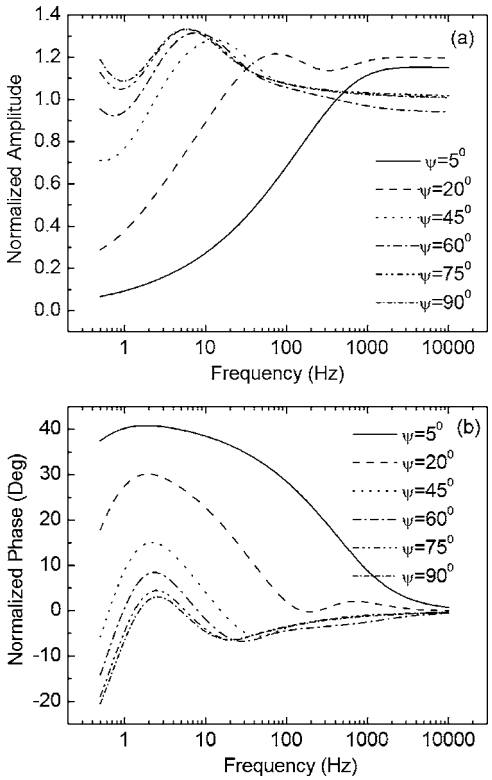

FIG. 5. The normalized surface thermal-wave amplitude and phase (measured at $r=R_0$ and $\theta=0°$) with different laser-beam sizes subtending different angles ψ, Fig. 1, for a sphere with a diameter of 3.0 mm. Both amplitude and phase plots use the same symbol notations for different angles.

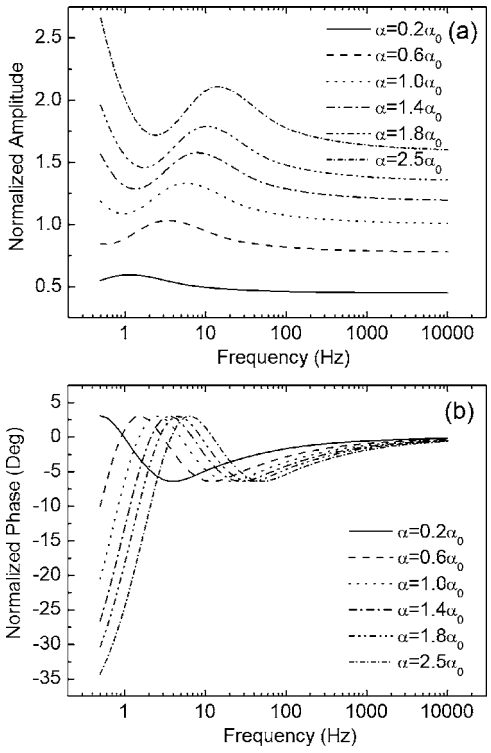

FIG. 6. Effect of thermal diffusivity of the material on the normalized surface thermal-wave amplitude and phase for a sphere with 3.0 mm diameter and measured at $r=R_0$, $\theta=0°$, and $\psi=90°$.

thermal waves. As the illumination aperture angle ψ decreases, the phase lead (with respect to the flat geometry) at the peak increases, again due to contributions from the remote spherical walls which retains the thermal-wave centroid closer to the upper surface detection point than in a semi-infinite flat geometry. In small-aperture cases, a larger phase lead is observed due to the fact that, albeit thermal-wave centroid confinement by remote curved interfaces moves deeper into the bulk of the solid, yet it remains closer to the observed surface point than in the semi-infinite flat-surface geometry. This is essentially an argument of the position of the thermal-wave centroid in three-dimensional versus one-dimensional geometries, as defined by the size of the illumination aperture. The normalized phase exhibits broadened width with decreasing ψ due to the increased relative contributions from more remote surface areas. At large values of ψ the surface locations are closer to the thermal-wave source and the interference pattern is readily visible. At higher frequencies, both amplitude and phase with different illumination angles ψ converges to that of a flat surface, i.e., normalized amplitude and phase toward 1 and 0, respectively, due to the shorter thermal diffusion length and the diminished role of curvature.

Figure 6 shows the effect of the thermal diffusivity of the material on the thermal-wave field measured at $\theta=0°$ for a solid with a 3-mm diameter and illumination angle $\psi=90°$. As the thermal diffusivity increases, the amplitude increases and the interference becomes more pronounced. This can be explained by the wider extent of the thermal wave into the spheroidal volume with increasing diffusivity, which includes contributions from a larger area of the curved interfaces to the ac temperature field at the observation point. The higher diffusivity enhances the contributions from interface-interacted thermal-wave fluxes to the overall field at the observation point thus exhibiting stronger interferometric behavior. This is corroborated by the phase interference pattern in Fig. 6(b): The increased thermal diffusion length with increased thermal diffusivity "sees" the confining curved interfaces at higher frequencies, therefore interference peaks also occur at higher frequencies. Therefore, the peak/trough frequency position of the thermal-wave field provides a unique feature for the determination of the thermal diffusivity of the material once the diameter is known.

IV. EXPERIMENTAL AND DISCUSSION

To verify the foregoing theoretical model, PTR experiments were performed using spherical ball-bearings as samples, made of SAE 52100 steel with composition: C 0.95%–1.05%, Cr 1.40%–1.65%, Si 0.15%–0.35%, P 0.025%, S 0.025%, Cu 0.25%, and Ni 0.30%. The sample diameters ranged from 4 to 13 mm. The experimental system is shown in Fig. 7. The thermal-wave source was a high-power semiconductor laser (~20 W). The output of the laser was modulated by a periodic current, the frequency of which was controlled by the computer and which also served as the lock-in reference. The beam was expanded, collimated, and then focused onto the surface of the sample with a spot size ranging from ~1 to 20 mm by adjusting the position of the lens. The harmonically modulated infrared radiation from the sample surface was collected by an off-axis paraboloidal

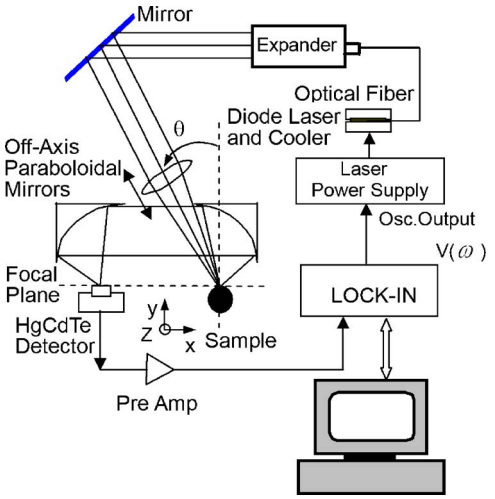

FIG. 7. (Color online) PTR experimental setup.

mirror system and detected by a HgCdTe detector. The signal from the detector was amplified by a low-noise preamplifier and then fed into a lock-in amplifier which was interfaced with a personal computer. The spherical sample was freely resting on a Teflon platform with a shallow notch to prevent the sample from rolling. Given that the contact area between the spherical sample and the platform was very small, Teflon is not a good thermal conductor and, most of all, the measurement point was usually far away from the bottom contact area (compared with the thermal diffusion length), the thermal effect of the sample-Teflon contact can be neglected.

The experimental setup was optimized using the similar procedure to that of the cylindrical sample.[7] The system was first optimized using a flat surface steel sample (not of the same material, because the one-dimensional PTR amplitude slope and phase frequency scans are independent of the material type[10]) such that both sample and detector were aligned onto the focal plane. This was done using a focused beam by adjusting the focusing lens and the *Y* direction of the flat sample, Fig. 7, since the crossing point of the focused beam with the flat surface matches, most sensitively, the focal point of the paraboloidal mirror system when the beam is focused. When the flat surface sample was replaced by a spherical surface, the thus determined focal plane was the optimized *Y* position for the spherical sample. Scanning the sample along *X* and *Z* (vertically) determined the optimized *X* and *Z* positions by maximizing the signal. By doing so, the crest of the curved surface of the sample (i.e., the point that is tangential to the focal plane) was exactly placed (within reasonable experimental error) at the focal point of the paraboloidal system. Therefore, the detector was monitoring the thermal-wave field emissions from that point. Synchronous thermal radiation information from other points on the sample surface can be neglected, which is especially true for our curved surface due to the strong defocusing (receding) effect of the curvature. Following this procedure, the laser beam was expanded to ~20 mm in diameter by moving the lens such that the laser beam was large enough to cover the entire hemispherical surface (i.e., ψ=90°) and also to validate the 1D model in the case of a flat sample.

Figures 8 and 9 show the experimental results and the

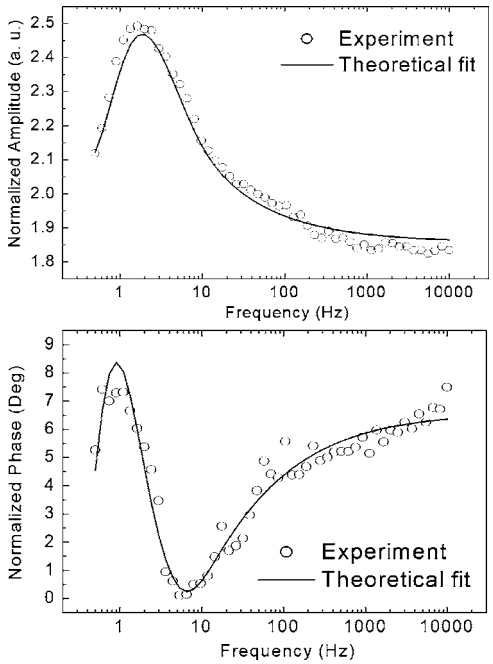

FIG. 8. Fitted results of amplitude and phase for a spherical steel sample with a diameter of 4.998 mm. Both amplitude and phase theoretical fits were performed using parameters measured from experimental phase data alone. The theoretical amplitude was calculated using the fitted parameters.

corresponding theoretical fits for two SAE 52100 steel spheres with diameter of 4.998 and 7.138 mm, respectively. The experimental data from the spherical ball bearings are normalized with the data from a C1018 steel flat surface to eliminate the instrumental transfer function. The fitting was performed using the phase data as the primary function in the

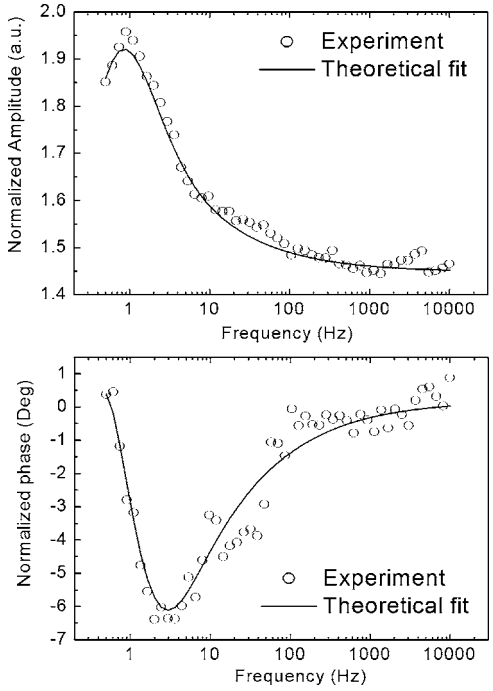

FIG. 9. Fitted results of amplitude and phase for a spherical steel sample with a diameter of 7.138 mm. Both amplitude and phase theoretical fits were performed using parameters measured from experimental phase data alone. The theoretical amplitude was calculated using the fitted parameters.

least square method because the phase is more sensitive to parameter changes than the amplitude. The corresponding amplitude data were calculated with the fitted parameters. Two parameters were introduced for fitting: thermal diffusivity and measurement angle θ. The purpose of introducing θ as a fitting parameter is that it allows taking into account the measurement angle due to the geometrical arrangement in the experiment, including the error of localizing the sample on the focal point in the experiment. The different behaviors shown in Figs. 3, 4, and 6 with respect to the measurement angle θ and the thermal diffusivity enable the multiparameter fitting process while preserving the uniqueness of the fitting parameters. The peak/valley magnitude difference remains unchanged when the thermal diffusivity changes (Fig. 6) while the same difference changes significantly with the measurement angle (Figs. 3 and 4). This fact is of great importance in practice, because it assures that one does not have to measure the actual incidence angle of the laser beam in order to obtain the thermal diffusivity.

Both results show good agreement between the experiments and the theoretical model. The best-fitted thermal diffusivities are 12.9×10^{-6} m^2/s and 12.6×10^{-6} m^2/s, respectively, calculated from Figs. 8 and 9 which are in excellent agreement with the literature value of 12.0×10^{-6} m^2/s.[16] The fitted measurement angle θ in Figs. 8 and 9 are 20° and 29°, respectively, which is consistent with the experimental arrangement in which the laser beam is incident on the spherical surface at an angle $\theta\sim30°$ as seen in Fig. 7. The discrepancy in θ obtained from Figs. 8 and 9 is probably due to operator induced alignment error. It should be pointed out that the noise in the normalized experimental data is mainly due to two sources: (1) Both spherical sample and flat reference sample were well polished, highly reflective sample surfaces. The absorption of the incident light was thus limited, resulting in relatively low signal-to-noise ratio. (2) The normalization process in both amplitude and phase statistically adds up the noises of signals from spherical and flat samples, thus aggravating the signal-to-noise ratio of the normalized signal. As shown in Figs. 8 and 9, the relative errors in amplitude and phase channels (defined as the ratio of the average deviation between the experimental data and the theoretical fits to the normalized amplitude and phase) are about 3% and 7%, respectively. Considering the fact that the frequency position of the peak/trough in both amplitude and phase are very sensitive to change in thermal diffusivity, the overall uncertainty of the fitting results of the thermal diffusivity and the angle have been estimated to be approximately 5%, i.e., the thermal diffusivity lies within the best fitted values above ±0.3 m^2/s.

V. CONCLUSIONS

We have formulated a new thermal-wave model that is suitable for characterizing spherical samples using laser infrared photothermal radiometry. Based on the Green function method, the thermal-wave field from a spherical sample with surface illumination from a laser beam with arbitrary spot size was obtained. The thermal-wave profile dependencies on various thermophysical and geometrical parameters were also investigated. In a manner similar to cylindrical solids, it was found that the thermal diffusivity of the material is the only thermophysical property involved in the frequency dependence of the thermal-wave field and it affects the pattern of thermal-wave interference within the body of spherical solids. The theoretical model was further validated by suitable experiments in which spherical steel samples with various diameters were measured and compared with literature values. Together with our earlier investigations on cylindrical solids,[7,8] this work complements the applications of the PTR technique in the two most commonly used curvilinear coordinate systems.

ACKNOWLEDGMENTS

The authors wish to acknowledge the support of the Ontario Centers of Excellence (OCE) and of the Natural Sciences and Engineering Research Council of Canada (NSERC) for this project. The support of the educational committee of Jiangsu province (Contract No. Q2108608) and an initializing research fund of Suzhou University to C.H.W. are gratefully acknowledged.

[1] P. E. Nordal and S. O. Kanstad, Phys. Scr. **20**, 659 (1979).
[2] R. D. Tom, E. P. O'Hara, and D. Benin, J. Appl. Phys. **53**, 5392 (1982).
[3] R. Santos and L. C. M. Miranda, J. Appl. Phys. **52**, 4194 (1981).
[4] M. Munidasa, T. C. Ma, A. Mandelis, S. K. Brown, and L. Mannik, J. Mater. Sci. Eng., A **159**, 111 (1992).
[5] L. Fabbri and P. Fenici, Rev. Sci. Instrum. **66**, 3593 (1995).
[6] L. Qian and P. Z. Li, Chin. Phys. **11**, 417 (1991).
[7] C. Wang, Y. Liu, and A. Mandelis, J. Appl. Phys. **96**, 3756 (2004).
[8] C. Wang, Y. Liu, and A. Mandelis, J. Appl. Phys. **97**, 014911 (2005).
[9] A. Salazar, F. Garrido, and R. Celorrio, J. Appl. Phys. **99**, 066116 (2006).
[10] A. Mandelis, *Diffusion-Wave Fields: Mathematical Methods and Green Functions* (Springer, New York, 2001).
[11] J. V. Beck, K. D. Cole, A. Haji-Sheikh, and B. Litkouhi, *Heat Conduction Using Green's Functions* (Hemisphere, Washington, DC, 1992), p. 11.
[12] H. S. Carslaw and J. C. Jaeger, *Conduction of Heat in Solids* (Oxford University Press, Oxford, 1959), pp. 20, 263.
[13] G. C. M. Meijer and A. W. Herwaarden, *Thermal Sensors* (Institute of Physics, Bristol, 1994), pp. 1–22.
[14] *Metal Handbook*, 10th ed. (ASM International, Materials Park, OH), Vol. 1, p. 196 (1990).
[15] J. Shen and A. Mandelis, Rev. Sci. Instrum. **66**, 4999 (1995).
[16] J. Zhang and A. T. Alpas, Acta Mater. **45**, 513 (1997).